Journal of Manufacturing Processes 131 (2024) 187–198

Contents lists available at ScienceDirect

Journal of Manufacturing Processes

journal homepage: www.elsevier.com/locate/manpro

Controlling heat accumulation through changing time per layer in laser powder bed fusion of nickel-based superalloy

Masahiro Kusano *, Makoto Watanabe

Research Center for Structural Materials, National Institute for Materials Science, 1-2-1 Sengen, Tsukuba 305-0047, Ibaraki, Japan

ARTICLE INFO

Keywords:
Temperature control
Laser powder bed fusion
Part-scale finite element thermal analysis
Time per layer
Nickel-base superalloy

ABSTRACT

Feedforward/feedback control of laser powder bed fusion (L-PBF) was proposed over a decade ago but remains challenging. Despite numerous parameters involved, most studies have attempted to control the process by changing laser power only. On the other hand, previous studies have shown that reducing the time per layer (*TPL*) increases the heat accumulation during the process. Thus, this feasibility study aimed to validate *TPL* as a potential parameter to control the top surface temperature of a nickel-based superalloy sample during L-PBF. First, a part-scale finite element thermal analysis with feedback control was performed to verify the temperature control strategy. Then, the sample was experimentally fabricated with the temperature control by changing *TPL*. The measured temperature was successfully maintained at target values (400, 500, and 700 °C), which were switched every 100 layers. In the as-fabricated IN738LC sample with the temperature control, the cellular microstructures coarsened by more than 0.5 μm and the hardness increased by approximately 50 HV as the target temperature was set higher. While demonstrating the potential of *TPL* for temperature control, its limitations in practical manufacturing were also discussed.

1. Introduction

Laser powder bed fusion (L-PBF), one of the metal additive manufacturing (AM) processes, can fabricate near-net-shape products by alternately spreading raw metal powder on a platform and selectively irradiating a laser beam to melt and solidify the powder layer. Such cyclic operations with local and fast solidification result in the formation of unique microstructures such as columnar crystal grains along the building direction composed of finer cellular sub-grains, which in turn determine the material properties of the as-fabricated product. Such interplays between processes, structures, and properties (P–S–P relationships) have been thoroughly investigated over the past decade. Indeed, in the case of the nickel-based superalloy Inconel 738LC (IN738LC) used as a model material in the current study, researchers have investigated the effects of process parameters including laser power P and scanning velocity v [1–3], hatching space h [3], scanning strategy [4], laser beam profile [5], pre-heating temperature [6], and time per layer (*TPL* [7], defined as the layer-wise time for powder spreading, laser scanning, and idling) on the microstructures and mechanical properties.

Among these process parameters, the previous studies [7–11] have experimentally and numerically revealed that *TPL*, sample geometry, and volumetric energy density (*VED*, defined as P/vhd where d is powder bed thickness) contribute significantly to the heat accumulation in the parts during the process. It should be noted that although there have been a number of studies on the effect of *TPL* (dwell time, idle time, inter layer time) on microstructures and mechanical properties of materials fabricated with direct energy deposition (DED) [12,13], studies of those with PBF are limited. In an experimental study by Mohr et al. [9], the measured top surface temperature of a 316L steel cubic sample increased more when the sample was fabricated with shorter *TPL* and larger VED in L-PBF. Referring to the study of Munk et al. [11] on the effects of sample geometry on the microstructure and mechanical properties of Ti-6Al-4V, Kusano and Watanabe [14] designed a constricted sample geometry that suppressed heat transfer to the baseplate during the L-PBF process, and successfully fabricated the constricted sample from Hastelloy X powder while holding it above 800 °C without using any preheating system. Their subsequent numerical and experimental study [7] revealed that shortening the *TPL* from 12.0 s to 8.5 s resulted in a top surface temperature of approximately 170 °C higher for IN738LC constricted samples. This is because the shorter the *TPL*, the less heat is lost from the built parts by reducing the extents of heat

* Corresponding author.
E-mail address: KUSANO.Masahiro@nims.go.jp (M. Kusano).

https://doi.org/10.1016/j.jmapro.2024.09.001
Received 3 June 2024; Received in revised form 6 August 2024; Accepted 1 September 2024
Available online 12 September 2024

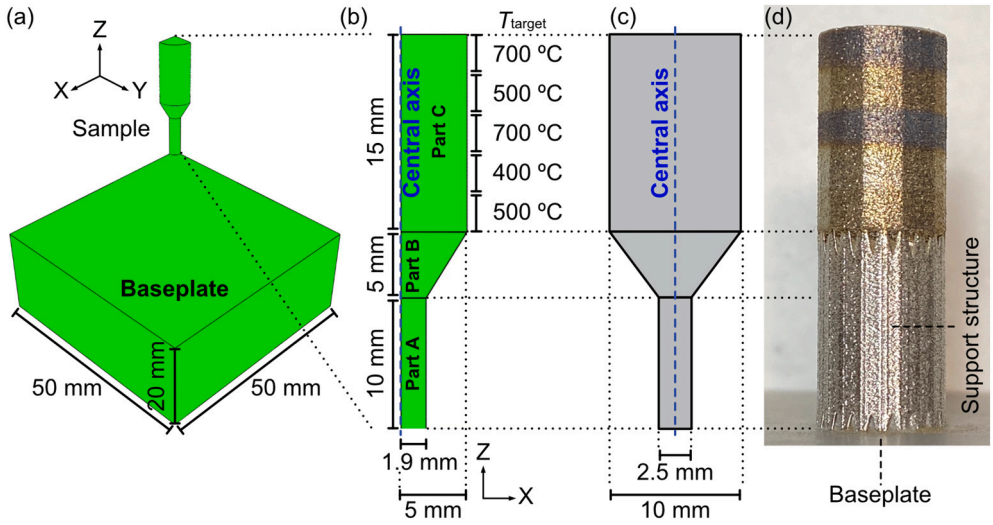

Fig. 1. Part-scale thermal analysis model with constricted geometries; (a) three-dimensional and (b) cross-sectional views. The target temperatures T_{target} for part C were also described in (b). (c) Dimensions and (d) photograph of the fabricated sample.

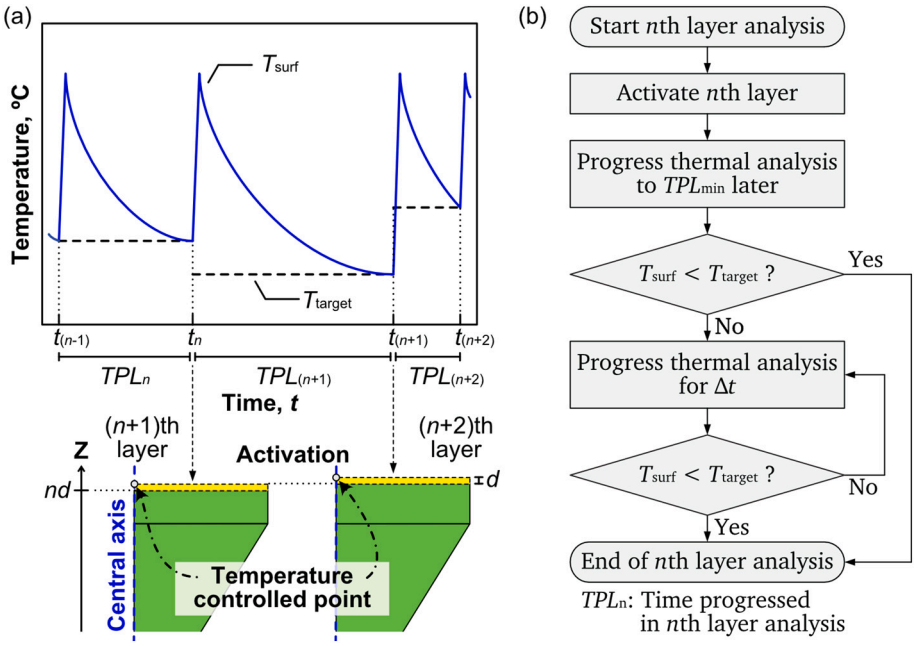

Fig. 2. (a) Schematic image of simulated temperature cycles on the top surface controlled above the target temperature T_{target}. The yellow parts in the bottom models indicate the $(n+1)$th and $(n+2)$th layers activated at t_n and $t_{(n+1)}$, respectively. (b) Flowchart to determine *TPL* in the part-scale thermal analysis. (For interpretation of the references to colour in this figure legend, the reader is referred to the web version of this article.)

Table 1
Process parameters for the part-scale thermal analysis and the experimental fabrication.

Symbol	Process parameter	Value	Unit
P	Laser power	300	W
v	Scanning velocity	1000	mm/s
h	Hatching space	100	μm
d	Powder layer thickness	30	μm

Table 2
Chemical composition of AMPERPRINT 0151.074 (wt%, Ni = balance).

B	C	N	O	Al	Si	P	S	Ti
0.007	0.10	0.008	0.017	3.5	0.02	0.005	0.002	3.5
Cr	Mn	Fe	Co	Zr	Nb	Mo	Ta	W
15.9	0.01	0.02	8.5	0.024	0.88	1.7	1.8	2.5

transfer to the substrate and surrounding powder bed, and forced convection and radiation on the top surface. Such heat accumulation significantly affects the microstructures and material properties of the as-fabricated parts [7–10,14]. Thus, to homogenize the as-fabricated microstructures and material properties, the part temperature should be stabilized through the process. Conversely, it is also expected that heat accumulation can be used to fabricate novel functionally gradient or site-specific materials. For these purposes, the L-PBF process should be controlled by changing the process parameters which traditionally have been fixed from the beginning to the end of fabrication.

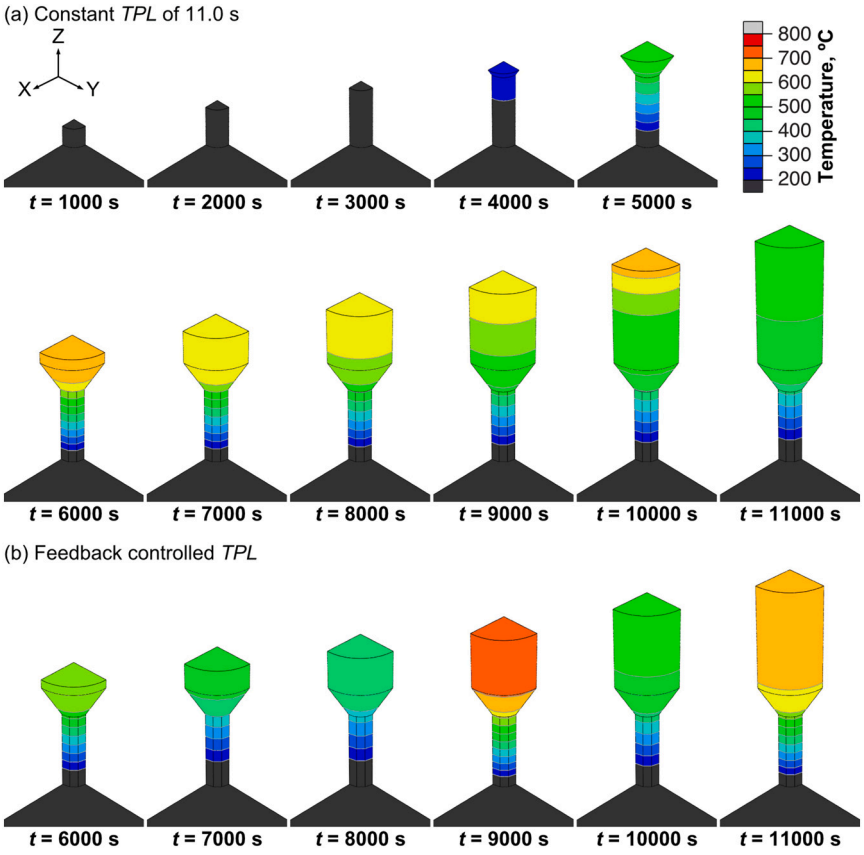

Fig. 3. The temperature fields simulated by the part-scale thermal analysis with (a) constant and (b) controlled *TPL*.

A concept for controlling the L-PBF process and its experimental feasibility were reported more than a decade ago by Craeghs et al. [15,16] and Rodriguez et al. [17]. Craeghs et al. [15,16] developed a control system to give feedback to the laser power based on a planar photodiode that was sensitive to changes in melting pool size. Due to their feedback control system, the top surface roughness of the built part was successfully improved over the conventional L-PBF process with constant process parameters. Such feedback control to the laser power based on optical monitoring of the melting pool has also been reported in recent years [18]. In addition, more advanced control of L-PBF has been reported utilizing numerical analysis and machine learning. Renken et al. [19] combined a closed-loop control strategy with a finite element model-based feedforward approach to reduce the temperature deviations of the melting pool in the L-PBF process. By providing feedback to the laser power, their approach successfully reduced the standard pyrometer signal by up to 90 % compared to the conventional process with constant laser power. Hussain et al. [20] developed a mathematical model for melting pool dynamics to design a feedback control system to minimize the effect of intertrack disturbance. The simulation results revealed that the designed controller regulated the desired melting pool shape in multiple laser scanning by modifying the laser power. Similarly, feed-forward control of laser power based on an analytical model has also been implemented to reduce over melting at the returning ends of the laser scan path [21]. Su et al. [22] have implemented closed-loop control to optimize the laser power in the DED process to stabilize the melting pool width, which fluctuates due to heat accumulation. This control promoted phase transformation and grain refinement in the deposited Fe-Ni-Cr alloy sample, resulting in the increase of tensile strength. In addition, Shi et al. [23] also suggested that such a closed-loop feedback system is essential in EB-PBF to reduce the defects to promote further applications.

While control strategies to stabilize melting pool geometry in laser scanning of one layer have been studied as described above, control of the sample temperature layer by layer has also been attempted. Rodriguez et al. [17] integrated a thermographic camera and a feedback system into a commercial electron beam powder bed fusion (EB-PBF) machine. In order to achieve more uniform surface temperature, the electron beam used as a heat source to melt the powder bed was controlled in-process by changing its scanning speed and current. This approach was further pursued by Mireles et al. [24], who successfully achieved a graded Ti-6Al-4V microstructure in a single part by changing the powder bed heating time prior to electron beam melting for each layer. Recently, finite-difference part-scale thermal analysis by Ren et al. [25] demonstrated that feed-forward control of laser power could hold the interlayer temperature of IN718 parts below 200 °C through the L-PBF process. To stabilize the sample temperature variation caused by the inverted pyramid geometry, Kavas et al. [26] applied closed-loop feedback control to the laser power. Although the temperature could be controlled within 2 % of the target value for some layers during the L-PBF process, it eventually became uncontrollable as the laser power was forced away from the stable range, leaving porosity in the fabricated parts. Riensche et al. [27] iterated a graph theory-based thermal simulation to optimize the laser power and *TPL* (dwell time) by predicting the thermal history of parts with various geometries through the L-PBF process, identifying layers with heat accumulation, and adjusting the process parameters. The optimized parameters successfully reduced heat accumulation, and the decrease in part temperatures resulted in narrower primary dendrite arm spacing (PDAS) of IN718 due to the increased cooling rate. In another study by Drendel et al. [28], on-board laser beam control based on finite element thermal analysis was successfully used to maintain the surface temperature within 20 K of the target value of 200 °C through the L-PBF process. Recently, Liu et al. [29] presented a concept of machine learning-enabled feedback loops for L-PBF, which is expected to allow efficient and effective decision

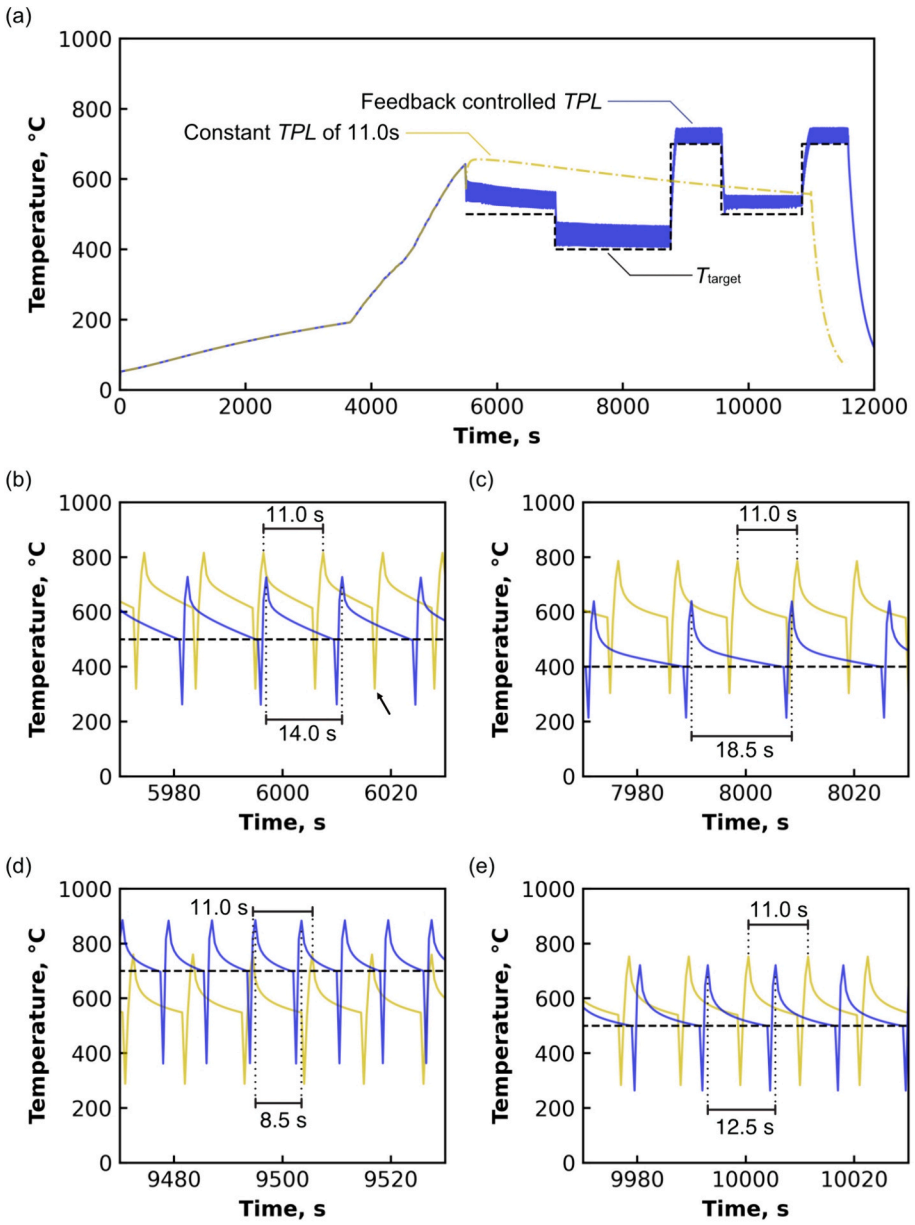

Fig. 4. The top surface temperature variations against the process time t simulated by the part-scale thermal analysis with constant and feedback-controlled *TPL*; (a) the whole process including cooling after the fabrication, (b) around 6000, (c) 8000, (d) 9500, and (e) 10,000 s. The black broken line indicates T_{target}. For (a), the top surface temperature was moving-averaged over 11.0 s. A black arrow in (b) indicates a temperature drop by the element activation for the subsequent layer.

making. Using a data-driven method, Kozjek et al. [30] predicted intra-layer variations in a representative temperature distribution that could be used for feedforward control.

In summary, even though L-PBF has many parameters to be changed depending on the situation, most studies have tried to control the process by changing only the laser power (or current for EB-PBF). Only the study by Riensche et al. [27] implemented control of *TPL* to avoid the heat accumulation. In addition, the target temperature in the previous studies was relatively low (e.g., 360 °C [26] and less than 200 °C [27,28]). On the other hand, depending on the process parameters and sample geometry, the top surface temperature could be higher than 500 °C due to heat accumulation [7,10,14]. Thus, such higher target temperature ranges should also be practically studied as target values for control to optimize the microstructures and properties.

The objective of the current study, therefore, was to validate *TPL* as a potential process parameter for feedback control of the elevated top surface temperature during the L-PBF process. Given that a sample with constricted geometry was to be fabricated by L-PBF from IN738LC powder, a part-scale finite element thermal analysis with a feedback control subroutine was first performed to verify the feasibility of the temperature control strategy (Sec. 3.1). Then, the actual sample was experimentally fabricated with the temperature control by changing *TPL*, and the top surface temperature was monitored in-process by a thermographic camera (Sec. 3.2). Finally, the microstructure and mechanical properties of the as-fabricated sample were evaluated (Sec. 3.3). While these results demonstrated the potential of *TPL* as a parameter for feedback control, some limitations exist in terms of practical manufacturing, and these are discussed in Sec. 4.

2. Materials and methods

2.1. Part-scale finite element thermal analysis

The constricted sample geometry for the thermal analysis and the

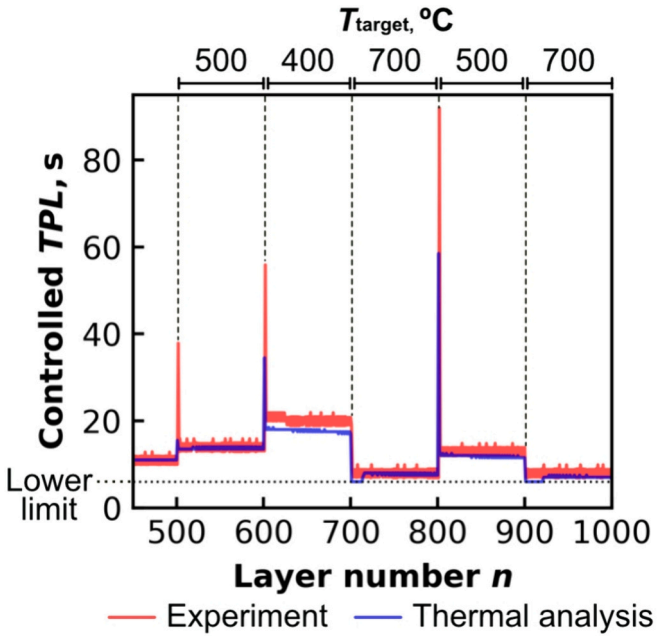

Fig. 5. Controlled *TPL* against layer number *n*. The blue line indicates the controlled *TPL* in the part-scale thermal analysis, and the red line represents the value in the experimental sample fabrication in Sec. 3.2. The black dotted line is the lower limit of *TPL* (6.5 s) in the thermal analysis. (For interpretation of the references to colour in this figure legend, the reader is referred to the web version of this article.)

fabrication shown in Fig. 1 (a–c) was identical to that designed in our previous study [7]. The part-scale thermal analysis was performed on a custom desktop computer with a CPU (Intel Core i7–7700K; Intel) using a finite element code Abaqus (ABAQUS/CAE 2022; Dassault Systems Simulia Corp.) to simulate the transient temperature field in the sample and substrate parts from the start to end of fabrication. The governing equation, boundary conditions, material properties of IN738LC and SUS304, and physical constants for the analysis were the same as those in reference [7]. In addition, by considering symmetry, the model can be reduced to one-fourth as shown in Fig. 1 (a), to save computational costs. The elements in the sample part were deactivated at the start of the thermal analysis and reactivated from the bottom per layer thickness according to the control strategy described below (birth and death method [7,13]). It should be noted that, as in reference [7], the support structures were actually fabricated below the overhang parts (see Fig. 1 (d)), whereas in the thermal analysis, instead, the radiuses of parts A and B were increased by an amount equivalent to the XY cross-sectional area of the supports (see Fig. 1 (b)).

Fig. 2 (a) shows a schematic image of the control of *TPL* from the *n*th to $(n+2)$th layers according to the sample top surface temperature. A flowchart in Fig. 2 (b) illustrates the algorithm to determine *TPL* or terminate the thermal analysis for *n*th layer. As indicated by the blue line in Fig. 2 (a), the top surface temperature T_{surf} repeats for each layer a rapid increase by laser scanning followed by a gradual decrease due to thermal diffusion. In the part-scale finite element thermal analysis, this process was modeled by newly activating the elements for the subsequent layer of thickness d (colored yellow in Fig. 2 (a)) and applying a heat flux there as laser scanning, and continuing to simulate the transient temperature field with thermal diffusion up to the subsequent layer activation. Therefore, in order to hold T_{surf} above the target value T_{target} (as indicated by the black broken lines in Fig. 2 (a)), the subsequent layer should be activated at the moment the temperature drops to T_{target}. In other words, if T_{target} is set lower/higher, *TPL* would be longer/shorter (see the $(n+1)$th and $(n+2)$th layers in Fig. 2 (a), respectively). Thus, the time t_n at which the process for the *n*th layer ends is expressed as follows:

$$t_n = \sum_{i}^{n} TPL_i \tag{1}$$

In the current study, while parts A and B were activated at a constant *TPL* of 11.0 s, the *TPL* for part C was feedback-controlled to hold the sample temperature above T_{target}, which was switched to 500 °C for layers 501–600, 400 °C for layers 601–700, 700 °C for layers 701–800, 500 °C for layers 801–900, and 700 °C for layers 701–1000 (corresponding to 3-mm intervals from 15 mm to 30 mm in height; see Fig. 1 (b)). For comparison, a thermal analysis with constant $TPL = 11.0$ s was also performed. The minimum value of time per layer $TPL_{\min}$ and time step Δt in Fig. 2 (b) were set to 6.5 s and 0.5 s, respectively. In addition, no upper limit was imposed on *TPL*.

As soon as the *n*th layer was activated, the heat flux $q_{laser,n}$ was applied as laser irradiation on the top surface of radius r and area A [7]:

$$q_{laser,n} = \begin{cases} \dfrac{\eta P}{A}, if\, t_{(n-1)} \le t \le t_{(n-1)} + t_{\text{scanning}} \\ 0, if\, t_{(n-1)} + t_{\text{scanning}} < t < t_n \end{cases} \tag{2}$$

$$t_{\text{scanning}} = \frac{2}{v}\sum_{k=1}^{N}\sqrt{2khr - (kh)^2} \tag{3}$$

$$N = \left\lfloor \frac{2r}{h} + \frac{1}{2} \right\rfloor \tag{4}$$

Here, P, v, and h are the laser power, scanning velocity, and hatching space, respectively (see Table 1). The variable η is the effective absorptivity, and was set to 0.5 as in the previous study [7]. Eq. (3) determines time t_{scanning} required to laser-scan a circle of r using a meander strategy with N tracks. The element activation, heat input, and subsequent idling were repeated from the first to 1000th layer, providing a transient temperature field in the sample and substrate through the process. The total time to complete the analysis without parallelization was less than 24 h. The analysis was validated in our previous study [7] by comparison with temperatures measured by a thermographic camera, which showed an error of 7.1±27.8 °C.

2.2. Experimental sample fabrication and observation

As shown in Fig. 1 (c, d), the constricted sample was fabricated on a stainless baseplate (98 × 98 × 20 mm^3) by a commercial L-PBF machine (SLM280; SLM Solutions GmbH) using IN738LC powder (AMPERPRINT 0151.074; Höganäs AB) as a raw material. Table 2 shows the composition of the raw powder provided by the manufacturer. The same process parameters for the part-scale thermal analysis in Table 1 were also used in the fabrication. The laser scanning strategy was a meander pattern, and the direction was rotated 67° per layer. The atmosphere in the chamber was replaced by argon gas so that the oxygen concentration was maintained to be less than 0.01 vol%.

The top surface temperature distribution of the building sample was monitored in-process by a thermographic camera (FAST M350; Telops Inc.). As in our previous studies [14,31], the camera was mounted on the outside of the L-PBF machine and measured the temperature field of the platform through a glass window (Si window with anti-reflective coating, Pier Optics Co., Ltd.) on the top of the chamber. The sampling rate and exposure time were 4 Hz (4 frames per second) and 100 μs, respectively. In the previous studies, the camera was properly calibrated by comparing the temperatures measured by thermocouples [14,31].

The L-PBF machine has a parameter, minimum scanning time t_{MinScan}, that is set to an integer greater than 0, and as the name suggests, changes the minimum time required for laser scanning. If t_{MinScan} is longer than t_{scanning}, an idling time t_{idling} $\left(= t_{\text{MinScan}} - t_{\text{scanning}}\right)$ will occur

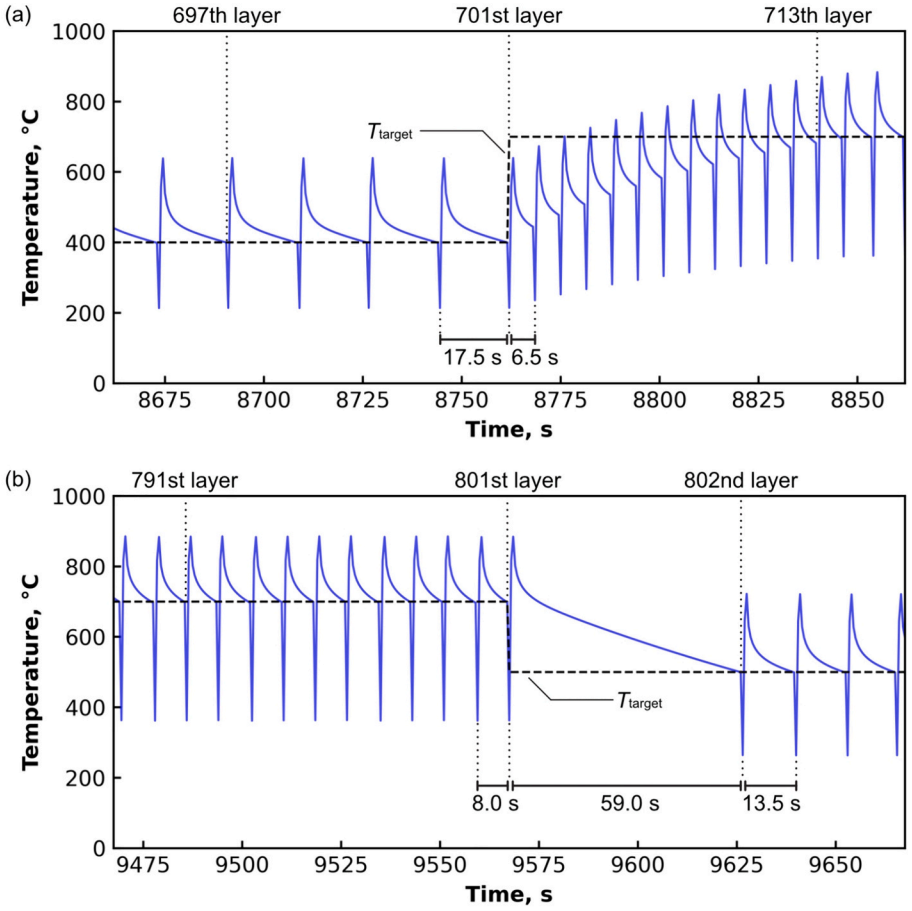

Fig. 6. The top surface temperature variations against the process time t simulated the part-scale thermal analysis with feedback control before and after switching T_{target} (a) from 400 °C to 700 °C at the 701st layer and (b) from 700 °C to 500 °C at the 801st layer.

after laser scanning. Since $t_{scanning}$ was at most 0.8 s for the constricted sample from eq. (3), a longer $t_{MinScan}$ will increase the idling time, resulting in a longer *TPL*. In the actual fabrication, *TPL* also includes $t_{spreading}$, the time taken for the powder spreading. Using these variables, *TPL* can be expressed as follows:

$$TPL = t_{spreading} + t_{MinScan} = t_{spreading} + t_{scanning} + t_{idling} \quad (5)$$

Due to the specification of the L-PBF machine, *TPL* has a variation greater than ±1.1 s even when $t_{MinScan}$ is set constant [7]. Thus, $t_{MinScan}$ was updated to keep the measured surface temperature close to the target value based on the same control strategy as the thermal analysis (Fig. 2), while also taking into account *TPL* predetermined by the thermal analysis. The actual value of *TPL* was logged on the L-PBF machine.

The as-fabricated sample shown in Fig. 1 (d) was cut at the XZ plane including the central axis, and the polished cross-sections were observed by a scanning electron microscope (SEM) (JSM-7200F; JEOL) equipped with an electron backscatter diffraction (EBSD) detector. After that, the cross-sections were electro-etched in the solution (12 ml H_3PO_4, 40 ml HNO_3, and 48 ml H_2SO_4 [32]) to observe the cellular microstructures within the grains. The Vickers hardness was also measured at three locations in the vicinity of the central axis, every 500 μm in height, by using a microhardness tester (AVK-A/AKASHI; Mitutoyo Corporation). The load and dwell time were 1.962 N and 15 s, respectively.

3. Results

3.1. Sample temperature control on part-scale thermal analysis

Fig. 3 shows the temperature field through the L-PBF process simulated by the part-scale thermal analysis. Fig. 4 (a) shows plots of T_{surf}at the central axis from the beginning to the end of the process, whereas Fig. 4 (b-e) shows the thermal cycles of the temperature over a shorter time range. It must be noted that the lines in Fig. 4 (a) represent moving averages over 11.0 s. When the sample part was built at a constant *TPL* of 11.0 s without feedback control (see Fig. 3 (a) and the yellow plot in Fig. 4 (a)), the sample and baseplate temperature fields were below 200 °C during the fabrication of part A. As part B was being built, T_{surf} was elevated sharply both by suppressing heat transfer through part A and by increasing the heat input per layer with the increase of the top surface area in part B. After part B was completed, T_{surf} reached over 650 °C, and then remained over 550 °C until the end of fabrication. As shown in Fig. 4 (b–e), the temperature increased sharply due to the heat input on the top surface, and gradually decreased until the subsequent element activation, which caused the temperature drop indicated by the black arrow in Fig. 4 (b). Such a thermal cycle was repeated every 11.0 s. This result was the same as in our previous study [7].

In contrast, the result when *TPL* was changed layer-by-layer to control the T_{surf} is also shown in Fig. 3 (b) and the blue plots in Fig. 4. The target temperature T_{target} is plotted as black broken lines in Fig. 4. Since the feedback control was not applied when fabricating parts A and B (in the range from 0 to 5500 s), the analysis results were the same as those under a constant *TPL* of 11.0 s. As shown in Fig. 4 (b)–(e), the element activation was successfully performed at the moment T_{surf} dropped to T_{target}. Fig. 5 shows the *TPL* against the layer number n. Since T_{target} was switched every 100 layers, *TPL* was controlled stepwise. In addition, as expected, the smaller T_{target} was, the longer *TPL* was.

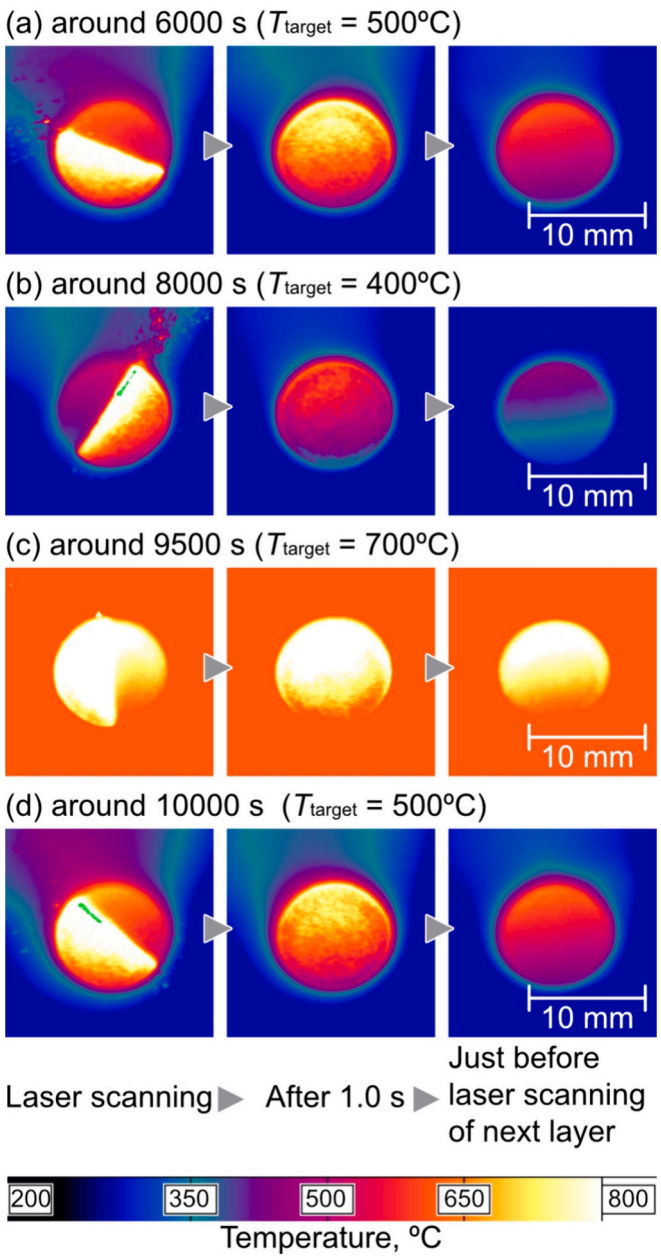

Fig. 7. Temperature distributions on the sample top surface measured by the thermographic camera; around (a) 6000, (b) 8000, (c) 9500, and (d) 10,000 s.

Furthermore, relatively long *TPLs* were set at the 501st, 601st, and 801st layers (see the corresponding spikes in Fig. 5). As shown in Fig. 6 (b), these longer *TPL* were adopted in order to wait for T_{surf} to drop to T_{target} switched from higher to lower. On the other hand, in the 701st and 901st layers, where T_{target} was switched from lower to higher, *TPL* was set at the lower limit of 6.5 s, which continued over the next 10 layers. This control was done to achieve a higher T_{target} by using the heat accumulation due to short *TPL*, as in the previous study [7]. As shown in Fig. 6 (a), T_{surf} gradually increased layer-by-layer after switching T_{target} from 400 °C to 700 °C.

In summary, the results of the feedback control on the part-scale thermal analysis indicate that when changing T_{target} from higher to lower, the process should be idled until T_{surf} drops to the set value. On the other hand, when changing T_{target} from lower to higher, *TPL* should be as short as possible until T_{surf} reaches the desired value in order to promote heat accumulation. It was also clarified that once the temperature reaches T_{target}, *TPL* does not need to be changed significantly thereafter.

3.2. Sample temperature control in experimental fabrication

The constricted sample was experimentally fabricated by the L-PBF machine by changing *TPL* based on the simulated results in Sec. 3.1. As shown in Fig. 1 (d), the sample was successfully fabricated, and the side colour differed about every 3 mm in height (every 100 layers), possibly because of the different degrees of oxidation during the process.

Fig. 7 shows the temperature distributions of the top surface during the process measured by the thermographic camera. The thermal history at the center of the top surface through the process can be readily seen by the red line in Fig. 8. As in Fig. 4, the results of the thermal analysis with feedback control and T_{target} are also indicated as blue lines and black broken lines, respectively. Again, the measured temperature in Fig. 8 (a) was moving-averaged over 11.0 s. The rapid temperature drops, an example of which is indicated by the black arrow in Fig. 8 (b), were caused by the passage of a recoater for spreading powder.

Throughout the sample fabrication, the temperature vs. time graph at the center point of the top surface of the sample, as shown in Fig. 8 (b-d), was updated at the sampling rate, and the value of t_{MinScan} was changed accordingly. As plotted by the solid red line in Fig. 5, *TPL* in the fabrication was controlled to values similar to those in the thermal analysis. In other words, when T_{target} was changed from higher to lower at the 601st and 801st layers, the building operations were paused until the surface temperature dropped to T_{target} so that *TPL* was extremely long, over 50 s. When T_{target} was changed from lower to higher at the 701st and 901st layers, $t_{\mathrm{MinScan}}$was set to the minimum value of 1 until the surface temperature reached T_{target}. During these other periods when T_{target} was constant, the value of t_{MinScan} was also almost constant. The total time for the fabrication with control was 3 h, 19 min, and 15 s, which is an increase of 16 min over the previous fabrication with a constant *TPL* of 11 s [7].

With this change in *TPL*, the temperatures just before laser scanning in Fig. 7 were almost close to T_{target}. As shown in Fig. 8 (a), the simulated and measured results were in good agreement up to around 8800 s, but after that, the time discrepancy between them became more pronounced (see the dotted lines for the 701st, 801st, and 901st layers in the figure). This is because, as evident in Fig. 5, *TPL* from the 601st to 700th layer was set to be about 2 s longer than simulated, which delayed the start of the 701st layer by about 200 s. Such *TPL* inputs longer than the simulated value caused the surface temperature to fall slightly below T_{target} as shown in Fig. 8(c).

Fig. 9 (a, b) shows the measured top surface temperature before and after switching T_{target} from 400 °C to 700 °C at the 701st layer and from 700 °C to 500 °C at the 801st layer, respectively. When T_{target} switched, it was possible to change the surface temperature as shown in this figure if *TPL* was set according to the strategy revealed by the thermal analysis. The temperature history before and after switching T_{target} also agreed well with that of the thermal analysis (see Fig. 6).

3.3. Microstructure and hardness

For the IN738LC sample fabricated with the temperature control, this section first presents the results of EBSD and SEM observations of its cross sections, followed by the results of Vickers hardness test. Fig. 10 (a) and (b) shows inverse pole figure (IPF) and kernel average misorientation (KAM) maps observed for each 3 mm height around the central axis of the as-fabricated part, respectively. As noted at the bottom of the figure, each of these heights corresponds to different T_{target} in the process. Among the various microstructural features extracted by the analysis software (OIM Analysis™ v8, EDAX), the mean value of KAM and the fraction of high angle grain boundary (HAGB) varied significantly (see the bottom of Fig. 10). In general, KAM is used as an indicator

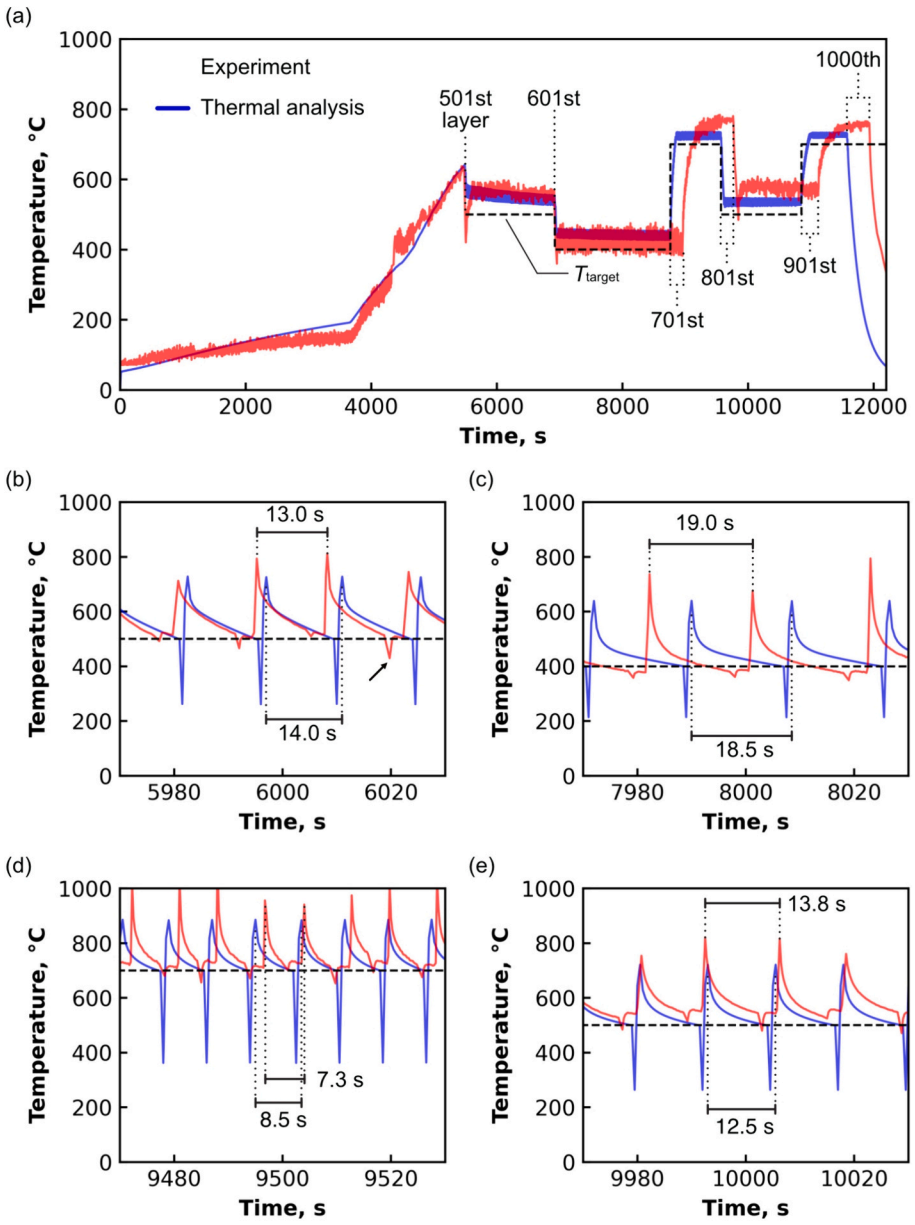

Fig. 8. The top surface temperature variations against the process time t measured by the thermographic camera (red lines); (a) the whole process including cooling after the fabrication, (b) around 6000, (c) 8000, (d) 9500, and (e) 10,000 s. The results of the part-scale thermal analysis with the controlled *TPL* and T_{target} are also shown as blue solid and black broken lines. As for (a), the top surface temperature is represented as a moving average over 11.0 s. A black arrow in (b) indicates the temperature drop by a recoater passing over the platform. (For interpretation of the references to colour in this figure legend, the reader is referred to the web version of this article.)

of strain concentration or the extent of deformation. As shown in Fig. 10 (f, g, i), KAM values with T_{target} of 400 and 500 °C are higher than 1.0 in most points. On the other hand, in the case of 700 °C (Fig. 10 (h, j)), KAM values were small inside some grains so that the mean value was relatively lower than that of 400 °C and 500 °C. In addition, the fraction of HAGB with crystallographic orientation differences greater than 15° was also relatively low at heights of 23–24 mm and 29–30 mm, which were fabricated with T_{target} at 700 °C. These trends are in good agreement with the results of EBSD of nickel-based alloy samples fabricated at higher temperatures in the preheating function of the L-PBF machine [6,33].

Fig. 11 shows SEM images around the central axis of the XZ cross section of the as-fabricated sample at different heights. As in the previous study [7], crystal grains consisting of very fine cellular structures were observed. As shown in Fig. 11 (e), a yellow square grid with 15.8 μm spacing was overlaid on this SEM image, and the widths of the cellular structure (primary dendrite arm spacing: PDAS) on each grid point was measured to obtain the mean and standard deviation of a total of 12 measurements per location. Fig. 12 shows a plot of the measured PDASs (red circles) against the sample height. For comparison, the PDASs for building at a constant *TPL* of 11 s [7] are also plotted as yellow hexagons. The dotted lines in the figure indicate the heights at which T_{target} was switched. When *TPL* was constant, the PDAS was nearly stable with respect to the sample height, although it deviated highly. On the other hand, when *TPL* was controlled, PDAS varied stepwise according to T_{target}. As in the previous studies [7,14], this was because the higher the top surface temperature, the lower the cooling rate in solidification, resulting in coarsening of the cellular structure. According to the finite element thermal analysis in laser beam scanning of the Hastelloy X sample [14], the cooling rates in the solidification were 3.5×10^5, 2.6×10^5, and 1.2×10^5 K/s for the initial sample temperatures of 400, 500,

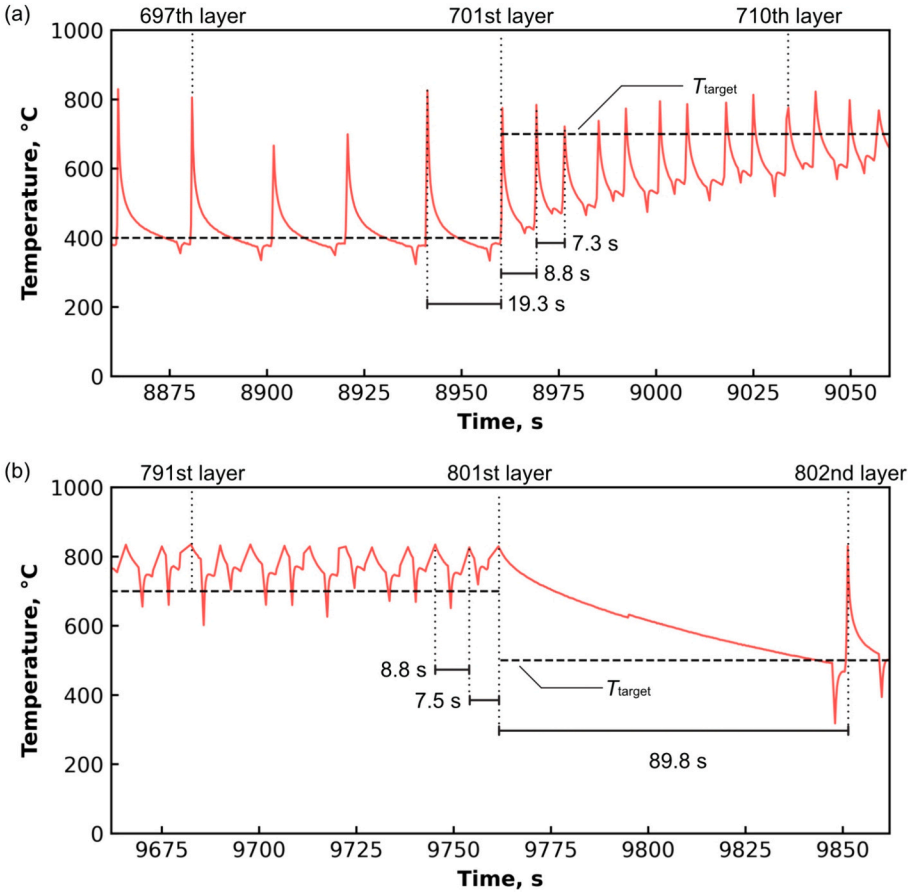

Fig. 9. The top surface temperature variations against the process time t measured by the thermographic camera before and after switching the value of T_{target} (a) from 400 °C to 700 °C at the 701st layer and (b) from 700 °C to 500 °C at the 801st layer.

and 700 °C. For nickel-based alloys including IN738LC, PDAS and cooling rate GR are related by the empirical equation $PDAS = a(GR)^{-b}$, where a was 50 μm, and b was 0.33 [34]. PDAS for each part, calculated using the equation, is also shown as blue lines in Fig. 12. From the figure, the measured PDAS tends to be larger than the calculated one, but the stepwise changes are in good agreement between them. This validates that the stepwise changes of PDAS are attributed to the cooling rate during solidification affected by the top surface temperature.

The Vickers hardness was also measured at three points around the central axis at each height, and plotted as red diamonds in Fig. 13. Again, the hardness for building at a constant *TPL* of 11 s in the previous study [7] was also plotted as yellow diamonds in the figure. Similar to PDAS, the hardness for constant *TPL* was stable regardless of sample height, whereas that for controlled *TPL* changed stepwise according to the switch in T_{target} every 100 layers. The change in hardness may have been due to the minute γ' particles, which were invisible even by SEM (see Fig. 11), being more precipitated at the elevated temperature, which would have resulted in hardening of the material. Indeed, in a study on the post-weld heat treatment of electron beam-welded IN738LC by Wang et al. [35], γ' precipitation took more than 30 and 10 min at 700 °C and 800 °C, respectively, whereas nanoscale γ' particles were found even at 1 min at temperatures above 900 °C. As described above for the study of ref. [14], the cooling rates in the solidification decreased with the increase of the sample temperatures. Furthermore, the measured PDAS, which increased with higher T_{target} (Fig. 12), also evidences a decrease in cooling rate. Such a decrease in cooling rate indicates that the top surface area was held above 900 °C for a longer period during the cooling process after laser scanning, which may result in the precipitation of γ'. Further observations (e.g., transmission electron microscope (TEM)) would reveal whether the precipitation of fine γ' particles in IN738LC is promoted by the elevated top surface during the process. In addition to the precipitation of γ', the changes in crystal grains and cellular structures with the temperature control may have contributed to the hardness, requiring further experiment and comprehensive discussion.

4. Discussion

The part-scale finite element thermal analysis and experimental L-PBF fabrication demonstrated that it is possible to control the top surface temperature of the building part by varying *TPL* during the process, resulting in changes in the microstructures and mechanical properties. As described above, when switching T_{target} from higher to lower, the L-PBF process should be idled until the top surface temperature drops to the intended value. On the other hand, when changing T_{target} from lower to higher, *TPL* should be kept as short as possible until the top surface temperature reaches the set value. Once the T_{target} is reached, *TPL* does not need to be changed significantly thereafter. With this strategy, the top surface temperature was successfully controlled to the set value in the experimental sample fabrication. For even more precise temperature control, *TPL* would need to be precisely controlled in the L-PBF machine. Indeed, the *TPL* of the commercial machine (SLM280) has a variation of ±1.1–1.7 s even when t_{MinScan} is set constant [7]. In addition, the machine is basically designed to build samples with constant t_{MinScan} so that the value can only be changed manually during the fabrication. Therefore, if *TPL* could be controlled more precisely and automatically based on the simulated or measured temperature filed, more precise temperature control could be achieved.

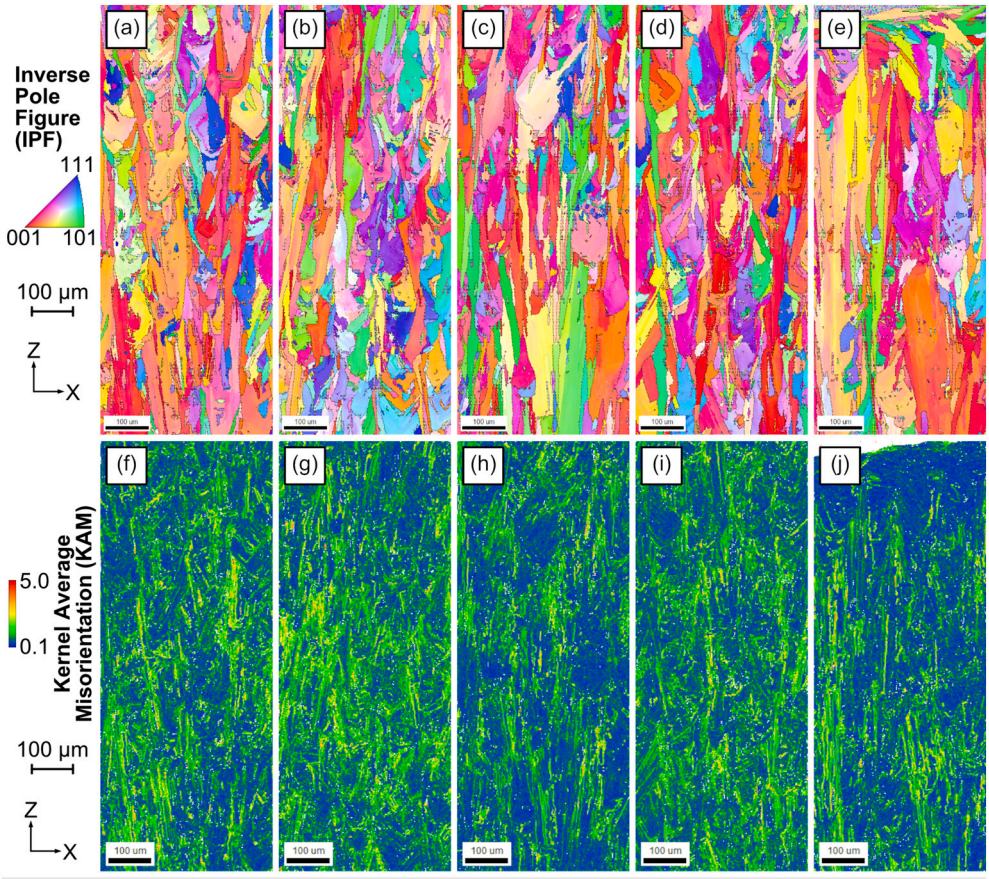

Height	17–18 mm	20–21 mm	23–24 mm	26–27 mm	29–30 mm
T_{target}	500°C	400°C	700°C	500°C	700°C
KAM	0.857	0.885	0.742	0.812	0.770
HAGB fraction	0.816	0.831	0.787	0.824	0.745

Fig. 10. Inverse pole figure (IPF) and kernel average misorientation (KAM) maps observed by EBSD at heights of (a, f) 17–18 mm, (b, g) 20–21 mm, (c, h) 23–24 mm, (d, i) 26–27 mm, and (e, j) 29–30 mm near the central axis of the fabricated parts, respectively. The reference direction of IPF is parallel to the Z axis (building direction). The average value of KAM and the fraction of high angle grain boundary (HAGB) as well as T_{target} corresponding to height are summarized at the bottom.

The controllable range of the top surface temperature is determined by the upper and lower limit of *TPL*. If the total process time is not a concern, the process for each layer can be delayed until the top surface temperature reaches an ambient temperature for each layer, although this approach is impractical. In practice, the total process time and upper limit of *TPL* are the constraints for setting the lower T_{target}. The lower limit of *TPL* is the shortest time for powder spreading and laser scanning. As in the previous study [7], such a shortest *TPL* will cause maximum heat accumulation, resulting in the highest temperature through the process. A part-scale finite element thermal analysis based on these constraints would estimate the controllable range of the top surface temperature. Such thermal analysis would also be useful for feedback control of the laser scanning conditions, and would help establish feedback control of the L-PBF process by revealing its feasibility and limitations in advance.

On the other hand, the modification of *TPL* must be more intricate when fabricating a part with more complex geometry or multiple parts with different geometries. It should be noted that cylinder part C of the constricted geometry (Fig. 1) was controlled in the current study so that the heat input per layer was constant during the process. On the other hand, to keep the material temperature constant when building a cone geometry like that of part B in Fig. 1 (b), *TPL* would also need to be continuously controlled for each layer because the heat input per layer changes with the top surface area. Riensche et al. [27] have already applied feedforward control by changing *TPL*, but they found that it was still challenging to maintain a constant temperature in complex geometry samples including such a cone part. In addition, since changes in *TPL* affect all parts on the baseplate, it would be difficult to control the temperature of multiple parts with different geometries at the same time. Moreover, it would be impossible to achieve temperature control by setting different target temperatures for each sample with the same geometry on the substrate. To achieve more flexible temperature control in fabricating multiple parts with complex geometry, it would be necessary to change not only *TPL* but also the laser scanning conditions for each part. In such simultaneous control of multiple process parameters, further consideration will need to be given not only to achieving target values, but also to avoiding defects such as porosity and microcracking.

5. Conclusion

In this study, the top surface temperature of the IN738LC constricted sample was successfully controlled by changing *TPL* during the L-PBF process. The part-scale finite element thermal analysis was useful to verify the feasibility of temperature control strategy. When switching T_{target} from higher to lower, the L-PBF process should be idled until the top surface temperature drops to the set value. On the other hand, when changing T_{target} from lower to higher, *TPL* should be as short as possible

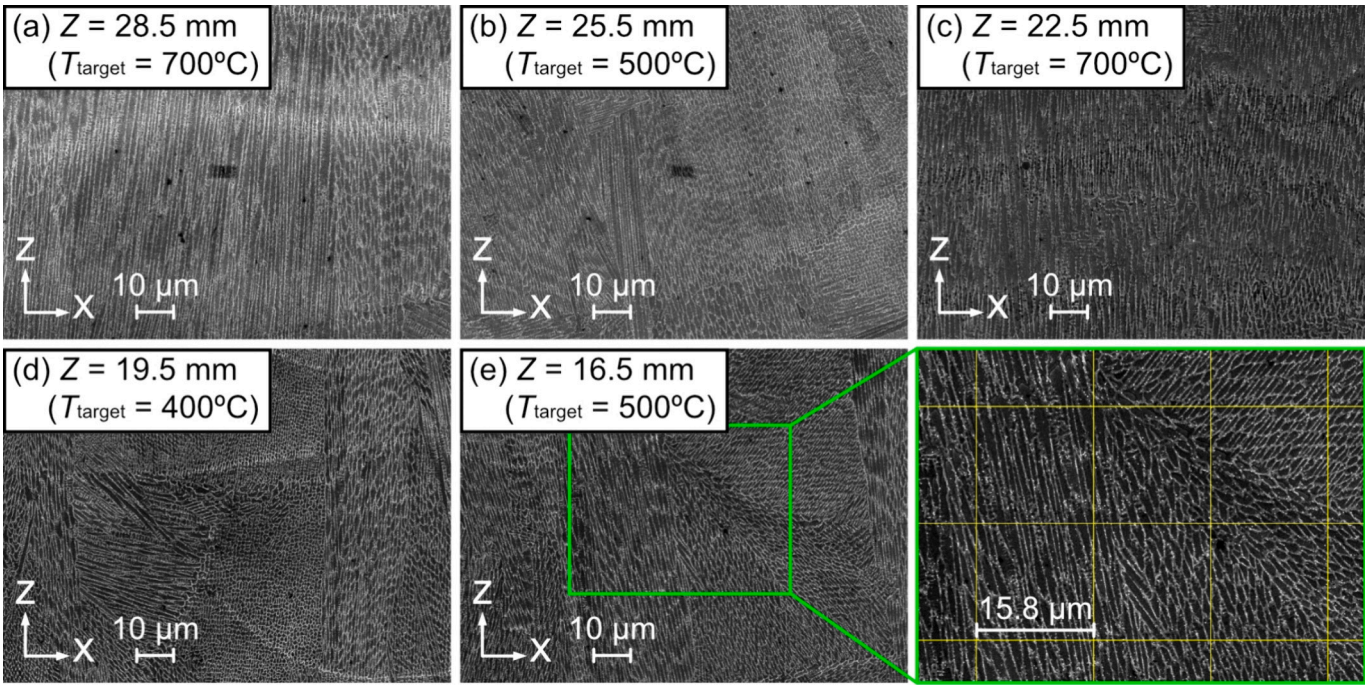

Fig. 11. SEM images around the central axis of the XZ cross section of the sample with controlled *TPL* at different sample heights *Z*: (a) 28.5 mm, (b) 25.5 mm, (c) 22.5 mm, (d) 19.5 mm, and (e) 16.5 mm. The yellow grid was overlaid as shown on the right in (e), and the width of the cellular structure was measured at each of its grid points. (For interpretation of the references to colour in this figure legend, the reader is referred to the web version of this article.)

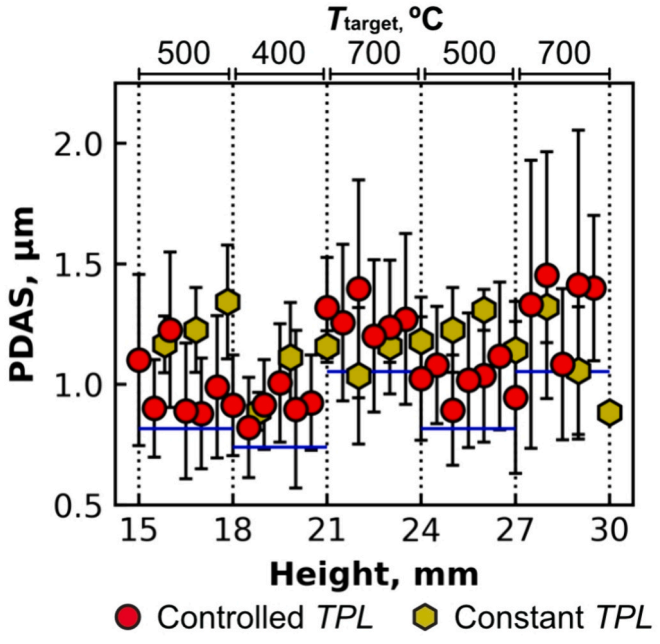

Fig. 12. The primary dendrite arm spacing (PDAS) with the sample height. The yellow hexagons indicate the PDAS for fabricating the same IN738LC constricted sample with a constant *TPL* of 11 s [7]. The error bars represent the standard deviations. The blue lines represent the calculated PADS using the empirical equation. (For interpretation of the references to colour in this figure legend, the reader is referred to the web version of this article.)

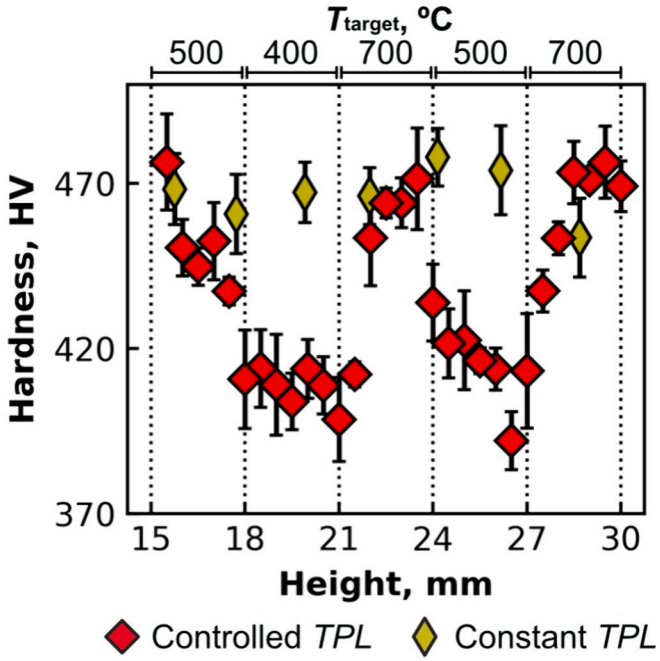

Fig. 13. A plot of Vickers hardness against sample height. The yellow diamonds indicate the hardness for fabricating the same IN738LC constricted sample with a constant *TPL* of 11 s [7]. The error bars represent the standard deviations.

until the top surface temperature reaches the intended value. In our fabrication of a cylinder part, once the T_{target} was reached, *TPL* did not need to be changed significantly thereafter, because the heat input per layer was constant throughout the fabrication process. Since T_{target} was switched in the range from 400 °C to 700 °C every 100 layers, the as-fabricated cellular structures and hardness also changed stepwise. Our results thus demonstrate that *TPL* is a candidate parameter for control of the top surface temperature during the process of homogenizing the microstructures and material properties or when creating a functionally graded or site-specific material.

CRediT authorship contribution statement

Masahiro Kusano: Writing – review & editing, Writing – original draft, Visualization, Validation, Methodology, Investigation, Funding acquisition, Formal analysis, Data curation. **Makoto Watanabe:** Writing – review & editing, Project administration, Funding acquisition.

Declaration of competing interest

The authors declare that they have no known competing financial interests or personal relationships that could have appeared to influence the work reported in this paper.

Data availability statement

The data that support the findings of this study are available from the corresponding author upon reasonable request.

Acknowledgements

This work was partly supported by the Cross-ministerial Strategic Innovation Promotion Program (SIP) “Materials Integration for Revolutionary Design System of Structural Materials” (funding agency: Japan Science and Technology Agency) and by JSPS KAKENHI Grant Number 23 K13583.

References

[1] Qiu C, Chen H, Liu Q, Yue S, Wang H. On the solidification behaviour and cracking origin of a nickel-based superalloy during selective laser melting. Mater Charact 2019;148:330–44. https://doi.org/10.1016/j.matchar.2018.12.032.
[2] Wang H, Zhang X, Wang GB, Shen J, Zhang GQ, Li YP, et al. Selective laser melting of the hard-to-weld IN738LC superalloy: efforts to mitigate defects and the resultant microstructural and mechanical properties. J Alloys Compd 2019;807. https://doi.org/10.1016/j.jallcom.2019.151662.
[3] Grange D, Bartout JD, Macquaire B, Colin C. Processing a non-weldable nickel-base superalloy by selective laser melting: role of the shape and size of the melt pools on solidification cracking. Materialia 2020;12. https://doi.org/10.1016/j.mtla.2020.100686.
[4] Xu J, Ding Y, Gao Y, Wang H, Hu Y, Zhang D. Grain refinement and crack inhibition of hard-to-weld Inconel 738 alloy by altering the scanning strategy during selective laser melting. Mater Des 2021;209:109940. https://doi.org/10.1016/j.matdes.2021.109940.
[5] Cloots M, Uggowitzer PJ, Wegener K. Investigations on the microstructure and crack formation of IN738LC samples processed by selective laser melting using Gaussian and doughnut profiles. Mater. Des. 2016;89:770–84. https://doi.org/10.1016/j.matdes.2015.10.027.
[6] Chen Y, Wang W, Ou Y, Li D, Chang H, Wu Y, et al. Effect of high preheating on the microstructure and mechanical properties of high gamma prime Ni-based superalloy manufactured by laser powder bed fusion. J Alloys Compd 2023;960:170598. https://doi.org/10.1016/j.jallcom.2023.170598.
[7] M. Kusano, Y. Takata, A. Yumoto, and M. Watanabe, Effects of time per layer and part geometry on thermal history and microcracking in the fabrication of nickel superalloy samples by laser powder bed fusion, additive manufacturing, Under review.
[8] Lui EW, Xu W, Pateras A, Qian M, Brandt M. New development in selective laser melting of Ti–6Al–4V: a wider processing window for the achievement of fully lamellar α + β microstructures. Jom 2017;69:2679–83. https://doi.org/10.1007/s11837-017-2599-9.
[9] Mohr G, Altenburg SJ, Hilgenberg K. Effects of inter layer time and build height on resulting properties of 316L stainless steel processed by laser powder bed fusion. Addit Manuf 2020;32:101080. https://doi.org/10.1016/j.addma.2020.101080.
[10] Chaudry MA, Mohr G, Hilgenberg K. Experimental and numerical comparison of heat accumulation during laser powder bed fusion of 316L stainless steel. Prog. Addit. Manuf. 2022;7:1071–83. https://doi.org/10.1007/s40964-022-00282-x.
[11] Munk J, Breitbarth E, Siemer T, Pirch N, Häfner C. Geometry effect on microstructure and mechanical properties in laser powder bed fusion of Ti-6Al-4V. Metals (Basel) 2022;12:482.
[12] Yadollahi A, Shamsaei N, Thompson SM, Seely DW. Effects of process time interval and heat treatment on the mechanical and microstructural properties of direct laser deposited 316L stainless steel. Mater Sci Eng A 2015;644:171–83.
[13] Denlinger ER, Heigel JC, Michaleris P, Palmer TA. Effect of inter-layer dwell time on distortion and residual stress in additive manufacturing of titanium and nickel alloys. J Mater Process Technol 2015;215:123–31.
[14] Kusano M, Watanabe M. Microstructure control of Hastelloy X by geometry-induced elevation of sample temperature during a laser powder bed fusion process. Mater. Des. 2022;222:111016. https://doi.org/10.1016/j.matdes.2022.111016.
[15] Mercelis, P., et al. “Feedback Control of Selective Laser Melting.” Proceedings of the 15th International Symposium on Electromachining, ISEM 2007, 2007, pp. 421–26.
[16] Craeghs Tom, et al. Feedback control of Layerwise laser melting using optical sensors. Physics Procedia 2010;5, no. PART 2:505–14. https://doi.org/10.1016/j.phpro.2010.08.078.
[17] Rodriguez, Emmanuel, et al. “Integration of a Thermal Imaging Feedback Control System in Electron Beam Melting.” 23rd Annual International Solid Freeform Fabrication Symposium - An Additive Manufacturing Conference, SFF 2012, 2012, pp. 945–61.
[18] Shkoruta Aleksandr, et al. Real-time image-based feedback control of laser powder bed fusion. ASME Letters in Dynamic Systems and Control 2022;2(2):1–7. https://doi.org/10.1115/1.4051588.
[19] Renken V, von Freyberg A, Schünemann K, Pastors F, Fischer A. In-process closed-loop control for stabilising the melt pool temperature in selective laser melting. Prog Addit Manuf 2019;4:411–21. https://doi.org/10.1007/s40964-019-00083-9.
[20] Hussain SZ, Kausar Z, Koreshi ZU, Sheikh SR, Rehman HZU, Yaqoob H, et al. Feedback control of melt pool area in selective laser melting additive manufacturing process. Processes 2021;9. https://doi.org/10.3390/pr9091547.
[21] Wang Q, Michaleris P(Pan), Nassar AR, Irwin JE, Ren Y, Stutzman CB. Model-based feedforward control of laser powder bed fusion additive manufacturing. Addit Manuf 2020;31. https://doi.org/10.1016/j.addma.2019.100985.
[22] Su Y, Wang Z, Xu X, Luo K, Lu J. Effect of closed-loop controlled melt pool width on microstructure and tensile property for Fe-Ni-Cr alloy in directed energy deposition. J. Manuf. Process. 2022;82:708–21.
[23] Shi Y, Gong S, Xu H, Yang G, Qiao J, Wang Z, et al. Electron beam metal additive manufacturing: defects formation and in-process control. J. Manuf. Process. 2023;101:386–431.
[24] Mireles J, Terrazas C, Gaytan SM, Roberson DA, Wicker RB. Closed-loop automatic feedback control in electron beam melting. Int J Adv Manuf Technol 2015;78:1193–9. https://doi.org/10.1007/s00170-014-6708-4.
[25] Ren Y, Wang Q. A finite difference method for fast prediction and control of part-scale temperature evolution in laser powder bed fusion. J. Manuf. Process. 2023;93:299–314.
[26] Kavas B, Balta EC, Tucker M, Rupenyan A, Lygeros J, Bambach M. Layer-to-layer closed-loop feedback control application for inter-layer temperature stabilization in laser powder bed fusion. Addit Manuf 2023;78:103847. https://doi.org/10.1016/j.addma.2023.103847.
[27] Riensche A, Bevans BD, Smoqi Z, Yavari R, Krishnan A, Gilligan J, et al. Feedforward control of thermal history in laser powder bed fusion: toward physics-based optimization of processing parameters. Mater. Des. 2022;224:111351. https://doi.org/10.1016/j.matdes.2022.111351.
[28] Drendel J, Logvinov R, Heinrichsdorff F, Hilgenberg K. Simulation-based controlling of local surface temperature in laser powder bed fusion using the process laser. Addit Manuf 2023;78:103854. https://doi.org/10.1016/j.addma.2023.103854.
[29] Liu C, Le Roux L, Ji Z, Kerfriden P, Lacan F, Bigot S. Machine learning-enabled feedback loops for metal powder bed fusion additive manufacturing. Procedia Comput Sci 2020;176:2586–95. https://doi.org/10.1016/j.procs.2020.09.314.
[30] Kozjek D, Porter C, Carter III FM, Mogonye J-E, Cao J. Data-driven prediction of geometry- and toolpath sequence-dependent intra-layer process conditions variations in laser powder bed fusion. J Manuf Process 2023;100:34–46.
[31] Kusano M, Kitano H, Watanabe M. Novel calibration strategy for validation of finite element thermal analysis of selective laser melting process using Bayesian optimization. Materials (Basel) 2021;14:1–21. https://doi.org/10.3390/ma14174948.
[32] Sanchez S, Smith P, Xu Z, Gaspard G, Hyde CJ, Wits WW, et al. Powder bed fusion of nickel-based superalloys: a review. Int J Mach Tool Manuf 2021;165. https://doi.org/10.1016/j.ijmachtools.2021.103729.
[33] Park J-H, Bang GB, Lee K-A, Son Y, Song YH, Lee B-S, et al. Effect of preheating temperature on microstructural and mechanical properties of Inconel 718 fabricated by selective laser melting. Met Mater Int 2022. https://doi.org/10.1007/s12540-022-01169-w.
[34] Iveković A, Montero-Sistiaga ML, Vleugels J, Kruth JP, Vanmeensel K. Crack mitigation in laser powder bed fusion processed Hastelloy X using a combined numerical-experimental approach. J Alloys Compd 2021;864. https://doi.org/10.1016/j.jallcom.2021.158803.
[35] Wang H, Han K, Peng F, Zhang B. Strain-age cracking in vacuum electron beam welded IN738LC alloy during post-weld heat treatment. Vacuum 2021;194:110588. https://doi.org/10.1016/j.vacuum.2021.110588.